Finite Elements in Analysis and Design 236 (2024) 104153

Contents lists available at ScienceDirect

Finite Elements in Analysis & Design

journal homepage: www.elsevier.com/locate/finel

Patient-specific numerical simulation of the bone healing process including implant materials and gait conditions

A. Martínez-Martínez [a,*], E. Nadal [a], D. Bonete [b], O. Allix [c], J.J. Ródenas [a]

[a] Institute of Mechanical and Biomechanical Engineering, Universitat Politècnica de València, Spain
[b] Fundación para la Investigación Hospital Universitario La Fe, Instituto de Investigación Sanitaria La Fe, Spain
[c] ENS Paris-Saclay, CNRS, LMT – Laboratoire de Mécanique et Technologie, Université Paris-Saclay, France

ARTICLE INFO

Keywords:
Treatment optimisation
Patient-specific simulation
Fuzzy logic controller
Finite element method
Bone healing
Callus healing

ABSTRACT

Numerical simulations in biomechanics, particularly in bone healing, present a cost-effective option compared to experiments that demand prolonged observations with human or with animal models. However, to define in-silico simulations of the bone healing process requires considering multiple factors, such as the implant design and patient's characteristics. As a result, the current challenge is integrating different numerical methodologies to simulate bone healing, aiming to facilitate the emergence of innovative clinical treatments and new implant designs.

In this paper, we present a patient-specific numerical methodology to simulate the bone healing process, able to consider patient's load conditions and bone density distribution provided by CT-scans. The main novelty is the combination of the Cartesian grid Finite Element Method (cgFEM) with a bone callus healing model, complemented by a load-condition optimisation scheme to relate implant materials and load conditions while ensuring successful healing outcome.

This numerical methodology creates a finite element model based on the patient's medical image, serving as a virtual testing tool for investigating the influence of implant materials on gait pattern requirements to ensure an optimal healing outcome. In practice, a personalised bone fracture model was employed to evaluate four distinct implant materials: two conventional materials (stainless steel and titanium) and two bioabsorbable candidates (polylactic acid plastic (PLA) and magnesium). The results offer personalised optimal load conditions for each studied material, showcasing the potential of in-silico studies in minimising uncertainties associated with exploring new clinical treatments.

1. Introduction

The healing process of long bone fractures (e.g. femur or tibia) is physiologically complex, involving biological and mechanical aspects [1]. There are two different healing processes: primary and secondary healing. Primary healing occurs when there is no movement between the bone fragments because they are tightly fixed. This kind of healing has no callus formation, and the bone fragments are healed directly [2,3]. On the other hand, secondary healing is the most common healing process for these injuries. It occurs when there is a small amount of motion in the fracture site [2], which provides of mechanical stimulus to fracture site. This crucial factor [4,5] leads to secondary bone formation through intramembranous and endochondral ossification. This stimulus is mainly determined by the physiological loads and the scaffold-bone interaction during the patient's gait [4,6–8].

* Corresponding author.
E-mail address: anmar29@etsid.upv.es (A. Martínez-Martínez).

https://doi.org/10.1016/j.finel.2024.104153
Received 27 November 2023; Received in revised form 13 February 2024; Accepted 14 March 2024
Available online 3 April 2024

Consequently, the mechanical features of the prosthesis and the applied loads are critical for the outcome of the healing process. During the implant design, it is necessary to consider both to ensure the success of bone healing and the mechanical integrity of the scaffold-bone system. There are two general strategies to study this process [1]: (1) experimental methods [9,10] and (2) numerical simulations [5,11–15]. The experimental phase allows studying healing under real conditions, but experiments are limited and more expensive than in-silico simulations and normally involve animal suffering. Once computational models are validated, we can create numerical tools to evaluate multiple scenarios considering the main parameters which govern the process or even the characteristics of patients.

In order to perform these computational simulations, several mechanobiological models have been presented in the last years considering biological and mechanical parameters of the bone healing process [5,11–15]. They update tissue concentrations according to the mechanical and biological magnitudes at the previous time step. These numerical models can be classified into two main groups. The first group computes tissue differentiation by solving nonlinear PDEs [11]. The second group mimics the mechanobiological healing process using a fuzzy logic controller (FLC) [5,12–15]. As a result, in this second group, solving any PDE to simulate the biological counterpart of the healing process is unnecessary. Shefelbine [16] presented the first model based on FL rules in 2005. Since then, more complete and accurate models have been developed, extending their range of application by considering other phenomena, model geometries or loading conditions.

These methodologies usually compute the mechanical magnitudes using traditional FEM techniques. However, the main limitation of these FEM approaches in medical applications is that they do not consider patient characteristics. As a starting point, they usually require building a CAD model of the bone based on a medical image and cannot easily consider the bone heterogeneity at voxel level. Recently, several Fictitious Domain Methods, such as Finite Cell Method [17], CutFEM [18] and cgFEM [19], circumvented these problems since they do not need any CAD model and naturally include the voxel-level bone heterogeneities in their formulation. These techniques have already demonstrated their potential in medical contexts [19–22].

Patient-specific simulations have been applied in different medical fields [23], including traumatology [24,25] to explore new clinical treatments. However, these techniques have not been combined with callus healing models. Nevertheless, patient-specific simulations of the healing process are crucial for implant optimisation since many factors influence implant design. For example, when bioabsorbable implants are considered, the amount of material should be minimised due to biocompatibility reasons while maintaining structural integrity and ensuring the healing process.

Currently, a primary challenge in this field is developing numerical methodologies that integrate various techniques considering the multitude of factors involved in the bone healing process. Therefore, the main objective of this work is to develop a numerical methodology based on the FEM for patient-specific simulations of the callus healing process able to relate the implant material and gait conditions during the treatment. The main novelty of this methodology is the combination of multiple numerical tools to finally create patient-specific numerical studies which provides insights into the relationship between implant materials and gait conditions.

This methodology combines the cgFEM implementation, which overcomes the limitations of traditional FEM techniques in medical applications, and a callus healing model based on FLC [12]. This numerical tool simulates the callus healing process using an image-based FEM model automatically created from the patient's medical image. Subsequently, an optimisation scheme is defined to relate implant materials and gait conditions looking for the maximisation of callus stiffness during the healing period. As a result, it is possible to study the effect of implant material properties on a customised optimal clinical treatment defined by the gait conditions.

The paper is organised as follows. Section 2 presents the methodology describing the cgFEM, FLC and how they are combined. Following this, we will explain the patient-specific case study and the results of applying a standard clinical treatment with a stainless steel implant in Section 3. Then, in Section 4, we will present an in-silico optimisation of gait conditions depending on implant material (stainless steel, titanium, magnesium and PLA). Finally, we expose the conclusions from the whole work in Section 5.

2. Methodology

In this section, we detail the methodology used to develop patient-specific simulations of the callus healing process. First, we present the mechanobiological problem to solve during the simulation. Since the mechanical stimulus is one of the main factors which governs the healing process, we use the FEM to solve the elasticity problem. The cgFEM technique provides the mechanical behaviour of the FEM model created from the patient's medical image. Then, we use a callus healing model from the bibliography [12] to obtain and update the mechanical properties of this model at each instant of the healing process. Finally, we describe how these techniques are combined to develop patient-specific simulations.

2.1. Callus healing process

In this work, we consider that the healing process of diaphyseal bone fractures (i.e. fracture in the shaft of a long bone) follows a secondary healing pattern. Briefly, this kind of healing process is governed by mechanical and biological parameters. Several numerical models have been developed to describe these phenomena considering mechanical stimuli and tissue concentration [11,26,27]. Most of these models consider only three kind of tissues inside the callus region [28]:

- Fibrous tissue: It consists of fibroblast and interstitial collagenous fibres. It is the weakest tissue with low stiffness. Initially, the callus region is composed of this tissue.
- Cartilage: It is an elastic material which is found around the callus region.

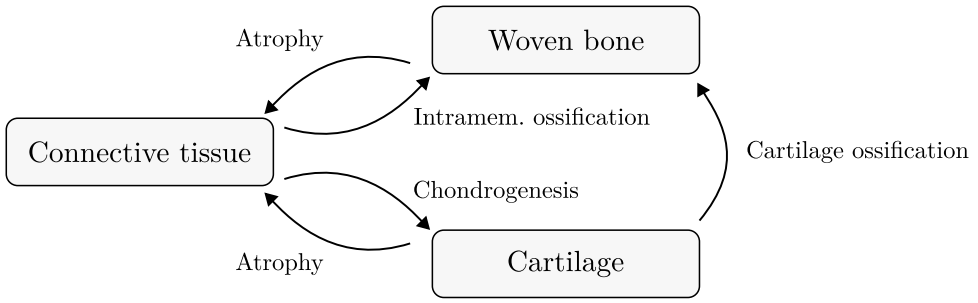

Fig. 1. Tissue differentiation mechanisms.

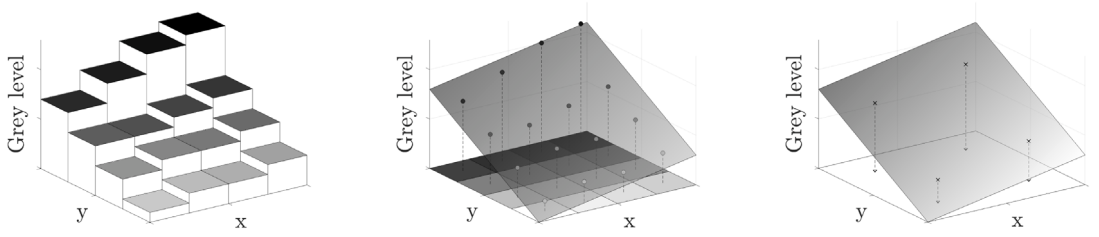

(a) Voxels' grey level distribution inside an element.

(b) Polynomial fitting to pixel values using the least squares method.

(c) Evaluation of the integration points on the fitted function.

Fig. 2. Application of the integration strategy based on least square fitting in a 2D element.

- Woven bone: It is built by osteoblasts, and it is the stiffest tissue responsible for bone bridging.

Tissue concentration depends on different biological processes which create and destroy cells, so increase or reduce tissue concentration along the healing period (see Fig. 1). The main mechanisms that rule tissue transformation are:

- Intramembraneous ossification: It consists of bone formation when mechanical stimuli and blood supply are adequate, and there is adjacent bone.
- Chondrogenesis: It is based on cartilage formation when there are high mechanical stimuli.
- Cartilage calcification. It is modelled as bone formation from cartilage tissue when there are high mechanical stimuli.
- Atrophy: Tissue destruction due to excessive strain.

As a result, it is necessary to define the numerical tools which allow describing this tissue differentiation and obtaining the variables which govern it: tissue concentration and mechanical stimulus.

2.2. Cartesian grid finite element method - cgFEM

In the linear elasticity problem, the aim is to find the displacement field $\boldsymbol{u}$, the strain field $\boldsymbol{\epsilon}$ and the stress field $\boldsymbol{\sigma}$ which fulfil the linear elasticity equations considering isotropic material behaviour. For this study, we employ cgFEM as a finite element solver due to its capability for the automatic generation of models based on medical images [19]. CgFEM, an in-house MATLAB-based software, has been employed in diverse numerical simulations [29], including applications within the domain of medical simulations, as documented in prior studies [19,22]. Additionally, a previous study [19] showed the accuracy of the method for image-based (i.e. voxel-based) simulations.

The cgFEM methodology originates at generating a FE model by embedding the geometry into a Cartesian mesh, i.e. the meshing domain $\hat{\Omega}$ is a rectangle in 2D or a cuboid in 3D, embedding the physical domain Ω. The domain integration strategy has been extended to the context of image-based modelling. A 3D image is a voxelization (pixelization in 2D) of a rectangular parallelepipedic domain that fits into the cgFEM meshing domain. Each Cartesian element contains a certain number of voxels, each of them is considered as a subdomain used to discretise the element. In cgFEM, to simplify mesh refinement, the number of voxels along each spatial direction of each element is forced to be $2^n, n \in \mathbb{N}$.

In this work, we use the integration strategy proposed by L. Giovannelli et al. [19] based on the least square fitting to capture the material heterogeneity of each element and to consider a certain level of the implicit anisotropy of the material distribution (see Fig. 2). For each element, the material properties are discretised by the several voxels/pixels contained inside of them (see Fig. 2(a)).

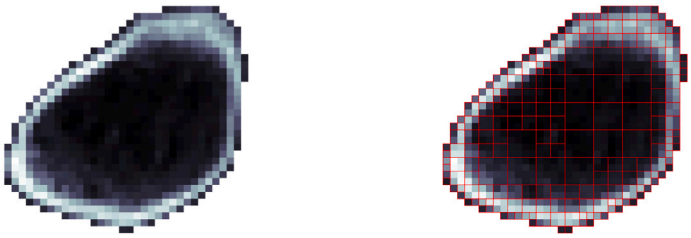

(a) Medical image of a tibia section.

(b) h-adapted mesh based on heterogeneity criteria.

Fig. 3. h-adaptive mesh performed in cgFEM where element boundaries are represented in red.

However, it is possible to fit a polynomial function to the greyscale values of the pixel/voxels (see Fig. 2(b)), which will capture the heterogeneity inside the element. As a result, the recovered material property field is piecewise continuous and discontinuous at the interface between elements. The new polynomial approximation to the material properties is considered in the integration of the stiffness matrix of each element using the proper Gaussian quadrature (see Fig. 2(c)). Conversely, elements where only one voxel is present do not follow the least square fitting technique presented. In that case, only the information of the unique voxel is available, so only those material properties are considered during the integration process.

2.2.1. h-adaptive cgFEM models

The h-adaptive refinement techniques allow increasing or reducing the number of elements in a mesh according to one or multiple established criteria. This makes it possible to transform a uniform mesh into an h-adaptive mesh where elements of different sizes can be found. This technique allows optimising the computational cost of FEM simulations.

In cgFEM, the meshing process is trivial even when performing h-adapted refinements. Basically, the refinement process is performed by partitioning elements in a nested way, resulting in child elements of the parent element (see Fig. 3). Conversely, the coarsening process consists on grouping some existing elements.

Particularly, in this paper we use a heterogeneity-based refinement criterion presented and validated by L. Giovannelli et al. [19]. This criterion defines a heterogeneity indicator for each element e as

$$I_R^e = \frac{\max\left(\alpha_i^{\Omega^e}\right) - \min\left(\alpha_i^{\Omega^e}\right)}{\max\left(\alpha_j^{\Omega}\right) - \min\left(\alpha_j^{\Omega}\right)}, \tag{1}$$

where α^{Ω^e} is the Young's modulus assigned to pixel i in the element domain Ω^e and α_j^{Ω} is the Young's modulus assigned to each pixel j in the whole image domain Ω. In our case, if I_R^e exceeds 0.2, the element is refined.

2.3. Callus healing model based on fuzzy logic

The callus healing process is characterised by a time evolution of tissue concentrations in the callus region, defining its mechanical properties. As a result, the simulation of this biological process poses an elastic problem that exhibits nonlinearity over time due to the dynamic changes in the mechanical properties of the callus throughout the healing process. The local update pattern of tissue concentration, and consequently mechanical properties, depends on the local mechanical stimuli and tissue concentration at each time step.

To model this process, we have implemented the mechanobiological model presented by T. Ren [12], based on fuzzy logic. This approach reduces the solving complexity of PDE-based models for simulating the bone healing process and provides more flexibility for continuous improvement, accommodating new experimental data as they become available. In practice, this model obtains and updates the mechanical properties of the FEM model at voxel level day by day. For this purpose, the FL-based model relates the governing variables (mechanical stimuli and tissue concretion) with the daily change in tissue concentration and mechanical properties. The time evolution of this process is integrated using an explicit time scheme considering a daily time step since the FL model is built accordingly. Previous authors inspire this numerical model [5,16], which is divided into two parts. First, a FLC locally determines tissue differentiation. Then, the local mechanical properties are obtained using a rule of mixtures, according to the tissue concentration.

It is important to note that while our approach integrates a previously developed model for healing process with our FEM numerical tool, this description of the healing model does not encompass all the intricate details of this methodology. The emphasis lies in presenting the fundamental concepts and explaining the adaptation process for the utilisation with the image-based models created using cgFEM. For a more comprehensive understanding of the model, consulting the original papers [5,12] is recommended, where the model is extensively presented including several hyperparameters and set of rules.

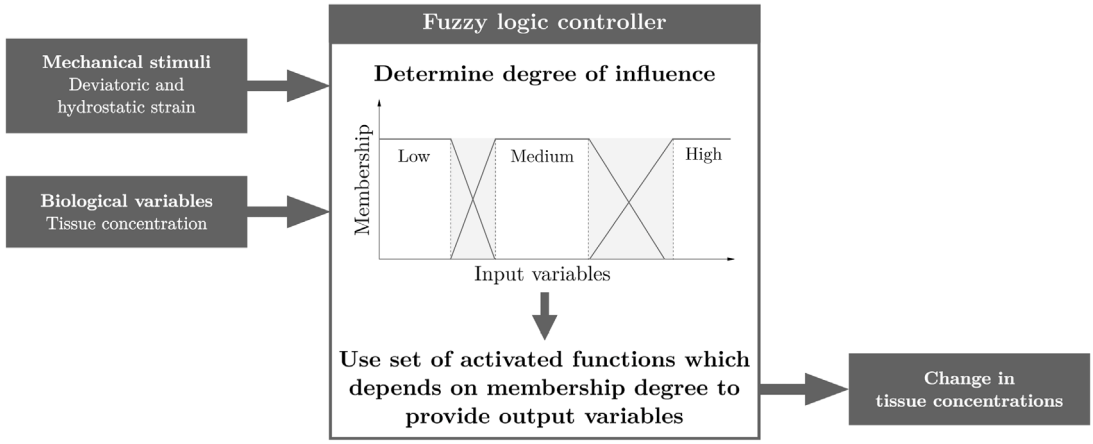

Fig. 4. Fuzzy logic controller which describes the tissue differentiation process during the callus healing day by day [5]. The input magnitudes are the mechanical stimuli and the tissue concentration. First, the degree of influence of each variable is computed using a membership function. It establishes a relationship between an input variable and its degree of belonging to a particular set (i.e. Low, Medium or High). Then, according to the FL rules, the value of change in tissue concentration is obtained as output variable.

Thus, the input variables represent three biological parameters and two mechanical stimulus values which govern the healing process and the output variables are the change in tissue concentration ($\frac{\partial c}{\partial t}$).

As a result, to compute de local tissue differentiation, the input variables in the FLC are:

- Tissue variables: element's bone and cartilage concentration (c_{bone} and $c_{cartilage}$), and maximum adjacent bone concentration ($c_{adj.bone}$).
- Mechanical variables: hydrostatic strain (ε_{Hydro}) and deviatoric strain (ε_{Dev}), which are defined in Eqs. (2) and (3), respectively.

$$\varepsilon_{Hydro} = \frac{1}{3}(\varepsilon_{xx} + \varepsilon_{yy} + \varepsilon_{zz}) \tag{2}$$

$$\varepsilon_{Dist} = \frac{\sqrt{2}}{2}\sqrt{(\varepsilon_{xx} - \varepsilon_{yy})^2 + (\varepsilon_{yy} - \varepsilon_{zz})^2 + (\varepsilon_{zz} - \varepsilon_{xx})^2 + 6\,(\varepsilon_{xy} + \varepsilon_{yz} + \varepsilon_{zx})^2} \tag{3}$$

Ren's model does not consider blood perfusion as a parameter in the FLC. In other words, it considers that the whole callus region is under optimal perfusion conditions. As a result, the initial day of the simulation represents the first day since the patient is authorised to apply load, not the first day from surgery.

After describing the variables considered in the process, Fig. 4 describes the workflow of the model as follows. The first step is using the FLC [30] to model the process. FLC is a type of control system that utilises fuzzy logic – a mathematical framework dealing with approximate reasoning and uncertainty – to model processes. FLCs are designed to handle imprecise or uncertain information, making them particularly suitable for applications where complex, nonlinear, or ambiguous conditions are present, such as the bone healing process. Particularly, in the approach we use [5,12], the main steps of this controller are:

- Fuzzification: This stage involves converting input variables (mechanical and biological) into fuzzy sets (i.e. Low, Medium or High). Fuzzy sets are characterised by membership functions that assign degrees of membership to different values. The function sets fuzzy limits that define the range of influence for each input variable. By assigning membership values within this range, the fuzzy logic system captures the imprecision and uncertainty inherent in these inputs, enabling a more nuanced representation of the tissue differentiation process during callus healing.
- Rule Base: The rule base contains a set of IF-THEN rules that express how the system should respond to various combinations of input variables. As in [12], in this case, 16 rules explain the biological phenomena presented in Section 2.1. For instance, if ε_{Dist} is VERY HIGH, then the atrophy phenomenon occurs, resulting in a decrease in bone and cartilage concentration.
- Inference Engine: The inference engine evaluates the rules based on the current fuzzy input values, determining the degree to which each rule is activated. It combines these rule activations to generate a fuzzy output, providing the change of tissue concentration (Δc).

Since a time integration scheme is necessary to update the tissue concentration over the callus healing [16]. The callus healing simulation follows a explicit Euler scheme (see Eq. (4)), as it was implemented by other authors [5,12]. Thus $\frac{\partial c}{\partial t}\Delta t \approx \Delta c$, using a time step of one day per iteration. Consequently, the applied load condition remains constant for each day. The output of the controller system is the change of tissue concentration on each voxel of the callus region, which allows computing the new c as

$$c_{i+1}(x_j) = \frac{\partial c}{\partial t}\,\Delta t + c_i, \text{ where} \tag{4}$$

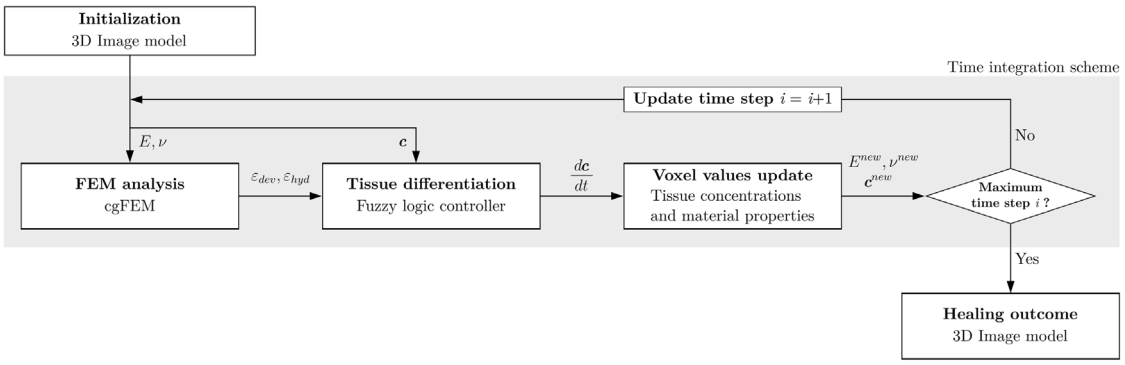

Fig. 5. Methodology's scheme where cgFEM is combined with FLC to perform the patient-specific simulation of the healing process.

$$\boldsymbol{c}_i(x_j) = \begin{pmatrix} c_i^{connective\ tissue}(x_j) \\ c_i^{woven\ bone}(x_j) \\ c_i^{cartilage}(x_j) \end{pmatrix}, \tag{5}$$

being j the voxel in Ω_c and k the tissue type.

The second stage of the model consists on obtaining the mechanical properties. We use a rule of mixtures [5] to obtain Young's modulus (E) and Poisson's ratio (ν) from the tissue concentration as follows:

$$E_i(x_j) = \sum_{k=1}^{3} E_k \cdot {\boldsymbol{c}_{i,k}}^3(x_j)\ \forall x \in \Omega_c, \tag{6}$$

$$\nu_i(x_j) = \sum_{k=1}^{3} \nu_k \cdot \boldsymbol{c}_{i,k}(x_j)\ \forall x \in \Omega_c. \tag{7}$$

In our methodology, all these numerical tools are combined as shown in Fig. 5. The process begins with the initial 3D image model of the bone and implant. First, the FE analysis is carried out with cgFEM and the predefined boundary conditions and loads. Then, the FLC provides the changes in tissue concentration according to the local tissue concentrations and mechanical stimulus. Then, we compute the tissue concentration of the next time step and the mechanical properties. If the stopping criteria are fulfilled, the simulation finishes. In this work, we only consider one stopping criterion, which is a maximum number of days to simulate. Conversely, the time step is updated and the process is repeated.

Additionally, this methodology has been validated for a normalised tibia fracture used in previous works [5,12] (see Annex).

3. Patient-specific case study

In this section, we will present the case study of this paper created from a medical image. Then, we will simulate the bone healing process of the customised model following a standard medical treatment as a validation procedure.

3.1. Patient-specific model

The case study is based on a CT scan of a tibia [31] from a patient whose body weight (BW) means an axial load of 700 N. Initially, this tibia was healthy and had no fracture. As a result, a preprocess is necessary to create an artificial fractured tibia image based on the original CT scan to develop our simulations.

3.1.1. Image preprocessing

Firstly, we have delimited a region of interest from the tibia with a total vertical length of 259 mm (see Fig. 6(a)). Then, that region is partially segmented. Most of the soft tissues surrounding the bone are removed, reducing the number of active elements of the mesh, in order to reduce the computational cost of the simulations. Additionally, in order to reduce the stair-case effect of the voxelized representation of the implant, the axis of the implant is aligned with the Z axis and the image is rotated and translated to properly model the implant into the medullary cavity. Then, we create an artificial fracture gap of 3 mm in the middle section removing voxels from the medical image.

The result of those modifications of the original medical image is shown in Fig. 6(b). The final image has a resolution of 1 mm per voxel and 256 voxels in each direction. The reference system is similar to other studies [32], with the sagittal plane defined by the YZ plane and the frontal plane as the XZ plane.

Then, a callus region is defined surrounding the gap with a maximum radius of 30 mm and a height of 70 mm (see Fig. 7). This region is initialised with fibrous tissue, and tissue differentiation will only be possible inside of it. Although the callus region

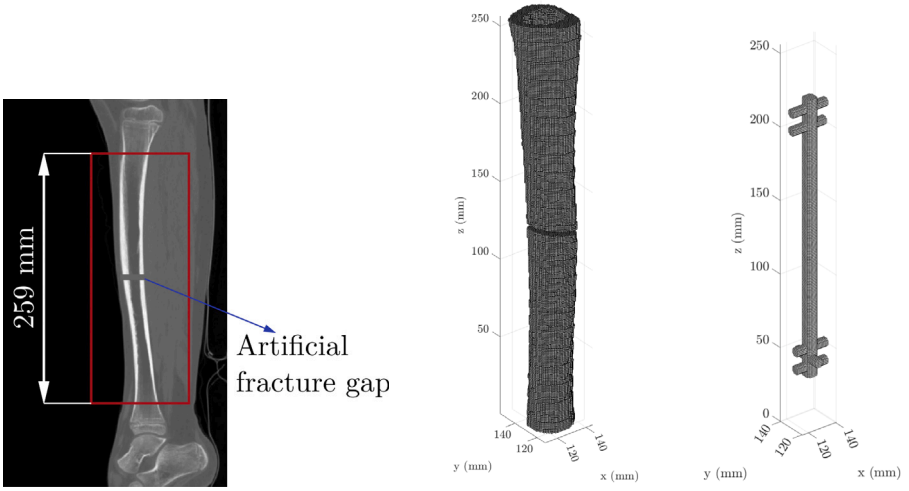

(a) Original tibia CT scan.

(b) Hard tissue from the processed CT scan.

(c) Image-based intramedullary nail.

Fig. 6. Preprocess of the medical image and implant design.

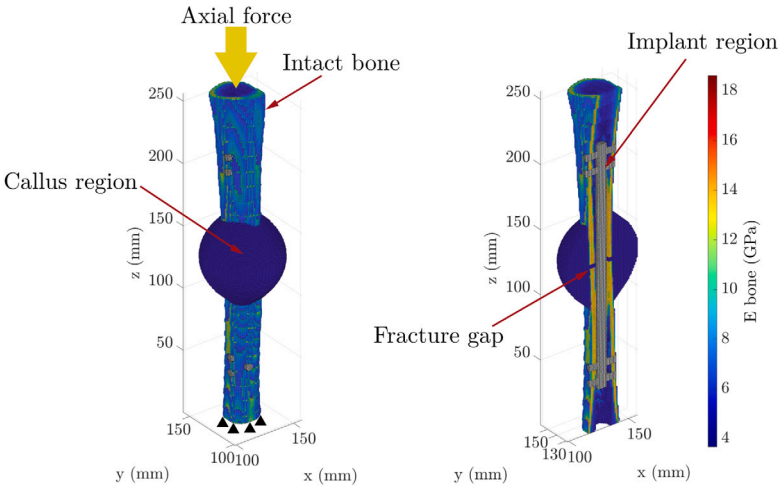

Fig. 7. Final image model of the fractured tibia with an intramedullary nail. Additionally, boundary conditions and domain regions are shown.

depends on each patient, and even on each fracture typology, the analysis can still be considered customised because shape and volume do not have a relevant influence on the results, according to previous sensitivity analysis [13,14] if it is sufficiently large. To ensure the validity of our simulations, we have verified that, in all cases, tissue differentiation does not reach the limits of this domain.

Finally, the image model is formed by three regions: the original medical image of the fractured bone, the callus healing region and the intramedullary nail.

3.1.2. Image-based implant fitting

In this case, we will consider an intramedullary nail inside the fracture tibia image (see Fig. 6(b)). We insert the geometry of the implant as a 8 mm diameter voxelized nail with 5 screws for fixation to the proximal and distal regions whose diameter is 5 mm as shown in Fig. 7. In this work, we consider the implant geometry as an image model for simplicity. As a result, the bone–implant model is entirely a 3D image.

Additionally, an extra air gap is set around the implant cylinder, between the prosthesis and the rest of the bone region, similar to a reamed intramedullary nail. Thus, contact between the implant and bone is avoided along the cylinder. Only the screws' voxels will fix the implant to the bone, considering a stick contact approach.

Table 1
Mechanical properties of the tissues in the callus healing region [5] and implant materials.

Material	Young's modulus E (MPa)	Poisson's ratio ν	Yield stress (MPa)
Woven bone	400	0.36	
Cartilage	200	0.45	
Connective tissue	3	0.30	
Stainless steel	193 000	0.30	800
Titanium	100 000	0.33	275
Magnesium	45 000	0.30	100
PLA	1280	0.36	60

3.1.3. Mesh parameters

An h-adapted mesh of 178 837 regular hexahedral trilinear elements is created for the image-based model with two element size levels. The finest element contains one voxel and its size is 1 mm. The coarsest element contains 2^3 voxels (i.e. 2 voxels per direction), and its element size is 2 mm. There are two refinement criteria to create this mesh: (1) Criterion based on the heterogeneity of the pixels contained in the element [19] (see Section 2.2.1) and (2) a predefined region of interest where the mesh is uniform and with the finer element size, in this case, the callus region.

Both refinement criteria have been chosen based on the characteristics of the healing problem. The callus region, where tissue differentiation occurs and material properties change over time, is the most critical and sensitive area. Consequently, the decision was made not to use an h-adapted mesh; instead, a fine uniform mesh was employed, with the correct element size ensured, as demonstrated in the sensitivity analysis of Annex A.6.

In the intact zone region, the voxel values represent CT-scan information that remains constant over time. For this reason, we have implemented the heterogeneity criterion presented by L. Giovanelli [19] to obtain an h-adapted mesh. The discretisation's impact on the healing outcome in this region is minimal compared to the callus region due to its consistently high stiffness, small cross-sectional size, and limitation to only two available element refinement levels. Consequently, it is possible to use this h-adapted mesh, which reduces the computational cost without undermining the accuracy of the model in terms of the healing outcome.

Additionally, to minimise the effect of the image resolution dependence in the callus healing model, we scale the FLC's outputs according to previous studies [5,12] as

$$\Delta c_{elem,\ bone} = \frac{L_{ref}}{L_{voxel}} \cdot \Delta c^{fuzzy}_{elem,\ bone}, \tag{8}$$

where L_{ref} is the maximum rate of new bone formation of 0.22 mm/day and L_{voxel} is the length of the hexahedral voxels used in cgFEM.

3.1.4. Boundary conditions

In this study, we will simulate the callus healing with an axial force defined as a percentage of the patient's BW. This load is applied in the proximal surface of the bone while nodal displacements from the distal region are fixed. Bending and torque forces are not considered in this study.

3.1.5. Material properties

Each of the three regions of the image model (callus region, bone image and implant) has different material properties. Table 1 shows the mechanical properties of the implant and the tissues of the callus healing region. Instead, the material properties of the bone are provided by the patient's image: each voxel of the medical image has a value in the Hounsfield unit (HU) scale. HU is a quantitative measure in computed tomography imaging to express the radiodensity of tissues, which is the ability to absorb radiation during medical image procedure. This magnitude is related to the mechanical properties of tissues. As a result, from those HU values and making use of the bone mineral density, different material properties can be assigned to each voxel [33].

Among the different expressions that can be found in the bibliography [34], we considered the following expression to obtain the bone apparent density (ρ_{app}) as a function of the HU values from the medical image

$$\rho_{app}(\mathrm{g/cm^3}) = 1 + 7.185\ 10^{-4}\mathrm{HU}, \tag{9}$$

presented in [35] for a femur bone and used in tibia simulations in [33]. Then, we define the ash density (ρ_{ash}), a quantitative measure widely utilised in the field of bone material characterisation [36,37], and convert ρ_{app} to Young's modulus (E),

$$\rho_{ash} = 0.6\ \rho_{app}, \tag{10}$$

$$E(\mathrm{MPa}) = 10\,200\ \rho^{2.01}_{ash}, \tag{11}$$

which were used in [38] in a tibia simulation. Additionally, the properties of possible implant materials are shown in Table 1 together with the material properties of the living tissues.

3.1.6. Numerical indicator: Interfragmentary movement

Interfragmentary movement (IFM) is the most common numerical indicator to assess the global stiffness of the callus healing over the treatment. It is computed as the difference in vertical displacement between a point on the upper surface of the fracture and its nearest point on the lower surface of the fracture [4,5]. In simple tibia models based on axisymmetric geometry, IFM is homogeneous over the bone section near the fracture gap when only axial force is applied [5,12]. However, in patient-specific models, bone and callus geometries and prosthesis interaction may cause a bending moment, resulting in a distribution of IFM over the fracture limit section.

For that reason, we propose a strategy to evaluate the IFM in patient-specific simulations. First, for each point A of the proximal fracture surface (upper section of the fracture) we detect the nearest point B in the distal fracture surface (lower section of the fracture). Then, we compute the difference in vertical displacement between each i pair of points. Finally, the IFM value is computed as the mean of the vertical displacement of the N_p pairs of points. Thus, IFM is computed for each time iteration of the simulation following the expression

$$\mathrm{IFM} = \frac{\sum_i^{N_p} u_z(x_{B_i}, y_{B_i}, z_{B_i}) - u_z(x_{A_i}, y_{A_i}, z_{A_i})}{N_p}. \tag{12}$$

3.2. Results from standard treatment

Once the fractured bone is fixed by the prosthesis, and vascularisation of the fracture region has been enhanced, the treatment mainly depends on the physiological loads applied during the following weeks. Nowadays, the most common implant materials to manufacture intramedullary nails are stainless steel and titanium. Walking as early as possible is recommended in this case, enhancing the mechanical stimulus since there is no risk of mechanical failure in these prostheses. Each patient and bone fracture may require different healing times, but the fracture is commonly bridged by woven bone in approximately 3 weeks from the load application.

In this study, we define a standard clinical treatment for a fractured tibia with a stainless steel intramedullary nail. In the base study, the axial load is 200% of the patient's BW for 60 days, equivalent to a patient with an injured leg who imperfectly walks [39]. Additionally, we have added two extra analyses with 180% and 220% of BW to study any possible sensitivity to this load condition. Fig. 8 shows the bone concentration evolution for the middle sagittal section of the bone. The IFM evolution over time is shown in Fig. 9. These results are related since the woven bone created in the callus region is the tissue type with higher stiffness. Therefore, as the bone concentration increases, the general trend is reducing the IFM.

This simulation considers the patient-specific geometry and stiffness distribution, so the healing process is heterogeneous around the fracture gap. The non-axisymmetric geometry and heterogeneous stiffness distribution of the bone cause a bending moment, hence, the mechanical stimulus is not homogeneous in the fracture section. Consequently, the healing pace is different for the regions around the gap (see Fig. 8). Moreover, this kind of high-stiffness implants exhibit a similar healing response when the axial load undergoes slight variations within the appropriate range for healing, which is compatible with clinical practice of high-stiffness implants.

This aspect explains the changes in the slope of IFM reduction (see Fig. 9). Finally, the time required to consolidate the fracture in this simulation is similar to actual clinical treatments for all the described numerical analyses. Hence, although further validation studies are necessary to derive highly accurate conclusions specific to patients, the potential of our numerical tool can be demonstrated through more complex virtual tests. These tests could explore the general trend of the relationship between gait conditions and implant designs.

4. A new patient-specific application: Finding the loads for an optimal healing process

Once the patient-specific methodology is developed (see Section 2.3) and tested for the standard treatment (see Section 3.2), the main aim is to use it as a virtual testing tool. Our methodology can perform in-silico studies to understand the healing process and to design the best treatment for each patient, which could not be done with just experimental methods. For that purpose, we present a patient-specific procedure to find the optimal treatment (physiological axial loads) according to a predefined set of time periods and implant design.

4.1. Callus healing optimisation scheme

The callus healing pattern depends on the mechanical stimulus, that is, on the loading pattern. Therefore, we will seek to determine the load pattern that optimises the callus healing process. In particular, the load pattern is defined by periods throughout the healing process in which the level of load to be applied by the patient is specified.

Consequently, we propose an optimisation scheme whose objective will be to find the physiological loads that maximise the callus stiffness at the end of each a priori given time interval. For each predefined time interval, the callus healing is simulated under an axial load X^n, which is the design variable of the problem. The objective function to be minimised is the IFM suffered by the bone represented by image (I) at the end of time period n in the healing process. It is crucial to note that we use IFM as an indicator of callus stiffness because it is a parameter commonly employed in bone healing research [4,5,12]. However, this distance measure only can be used as a comparison magnitude if it is evaluated using the same load value. Otherwise, the resulting IFM

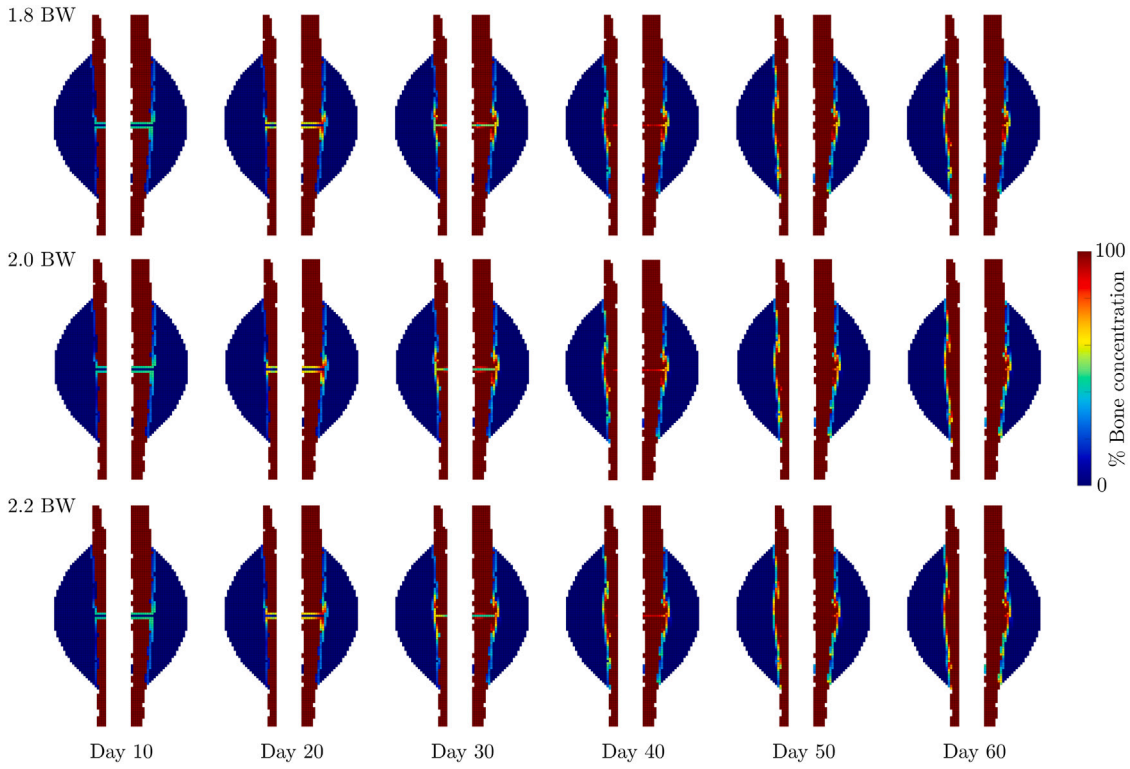

Fig. 8. Evolution of bone concentration in a section of the sagittal plane for different loading conditions.

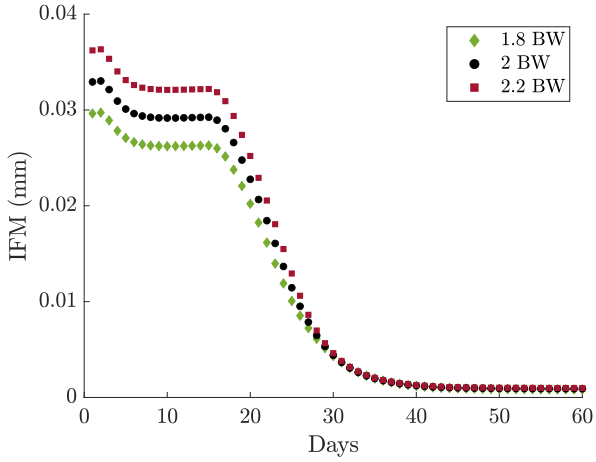

Fig. 9. IFM evolution for the simulation of a standard treatment with a stainless steel implant and a constant axial force of 1.8, 2 and 2.2 times de patient's BW over time.

value at each analysis would not represent the callus stiffness in the same way. Consequently, when comparing various numerical studies, it becomes essential to consistently assess the IFM under the same load conditions.

To address this consideration, we propose a standardised evaluation of the IFM using a consistent reference load denoted as X_{ref} (in our study, $X_{\text{ref}} = 3\,\text{BW}$) across all time periods and analyses. As a result, regardless varying the applied loads (X^n) during the healing process, IFM values used to evaluate callus stiffness are always computed using this fixed reference load. This standardised approach allows us to relate the IFM solely to callus stiffness, eliminating the dependence on X and facilitating meaningful comparisons between different studies.

Thus, the optimisation problem is

$$\begin{aligned} &\min_{X^n} : && \text{IFM } (I^n_{end}, X_{ref}) \\ &subject\ to && X^n_{lower} \leq X^n \leq X^n_{upper} \quad n = 1, N \end{aligned} \tag{13}$$

where the number of time intervals (N) and their duration (t^n_{ini}, t^n_{end}) is defined at the beginning of the process, for example, according to the planned medical check-ups.

Algorithm 1 Clinical treatment optimisation algorithm

```
Load initial image I_0
I^0_opt = I_0
Define N intervals and their duration t_ini and t_end
for n = 1, N do
    I^n_ini = I^{n-1}_opt
    Initialize Exploration=1
    Initialize optimiser counter j = 0
    Define exploration range X^n_lower and X^n_upper
    while Exploration do
        Update counter j = j + 1
        Define load to apply X^n_j according to the optimisation algorithm
        Run Callus Healing Process from t^n_ini to t^n_end and obtain I^j_end
        Evaluate objective function IFM for X_ref
        if StopCriterion is reached then
            Update I^n_opt = I^j_end
            Exploration = 0
        end if
    end while
end for
```

Algorithm 1 represents the optimisation process to find the best load values using the patient-specific healing methodology (FLC and cgFEM). In this work, the proposed algorithm has two parts. First, a greedy optimisation scheme is used to find an optimal group of physiological loads for the healing process with fewer objective function evaluations. Thus, the optimisation procedure is carried out for each predefined time interval, computing the local optimal load. In other words, in the first time step, the initial image model (I_0) is the original fractured bone image. Subsequently, for the succeeding time intervals, the initial image model is based on the optimal result obtained from the preceding time interval.

The second part is the exploration of the objective function at each period. In this work, we have chosen a Bayesian optimiser to explore the design domain with a maximum of 20 iterations/samples, so the stopping criterion is reaching the maximum number of iterations. In the exploration phase, only those samples where the maximum von Mises stress in the implant region does not exceed the yield stress limit are considered to be feasible samples (see Table 1). The result of this process will be the optimal configuration of loads whose outcome is a final bone image model with minimum IFM. Note that other optimisation algorithms could be considered instead of the Bayesian optimiser.

4.2. Optimisation problem

To optimise the clinical treatment, some parameters must be predefined. Clinical experts should specify these parameters to ensure the relevance of the analysis results. In this study, the treatment is divided into two intervals where the callus stiffness will be maximised (see Fig. 10). The first time interval goes from day 1 to 30 ($t^1_{ini} = 1$ and $t^1_{end} = 30$), and the second one goes from day 31 to 60 ($t^2_{ini} = 31$ and $t^2_{end} = 60$). In order to limit the exploration range of the algorithm, in the first time interval, the maximum physiological load value is 2 BW (equivalent load to abnormal walk [40,41]), and in the last time interval is 3 BW (equivalent load to normal walk [40,41]). For both time intervals, the minimum load value to explore is 0.01 BW. Additionally, the reference compression axial load X_{ref} used to evaluate the objective function is defined as 3 BW in all the studies.

In this study, we consider the implant–bone model presented in Section 3.1 evaluating four implant materials (stainless steel, titanium, magnesium and PLA) and maintaining the same geometry. Steel and titanium are currently used in long-bone fracture treatments but require extraction surgery once the bone has healed. However, magnesium and PLA are bioabsorbable materials (BM) [42] and may be degraded and absorbed after months or years. The mechanical properties of BMs are different from stainless steel or titanium [43], so this study will identify the influence of implant material stiffness (see Table 1) on the patient's optimal treatment.

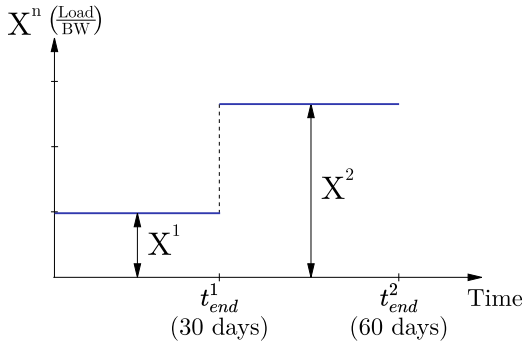

Fig. 10. Definition of the optimisation problem with two time periods. As a result, there are two optimal load values to find (X^1 and X^2)., which are constant over time of each period.

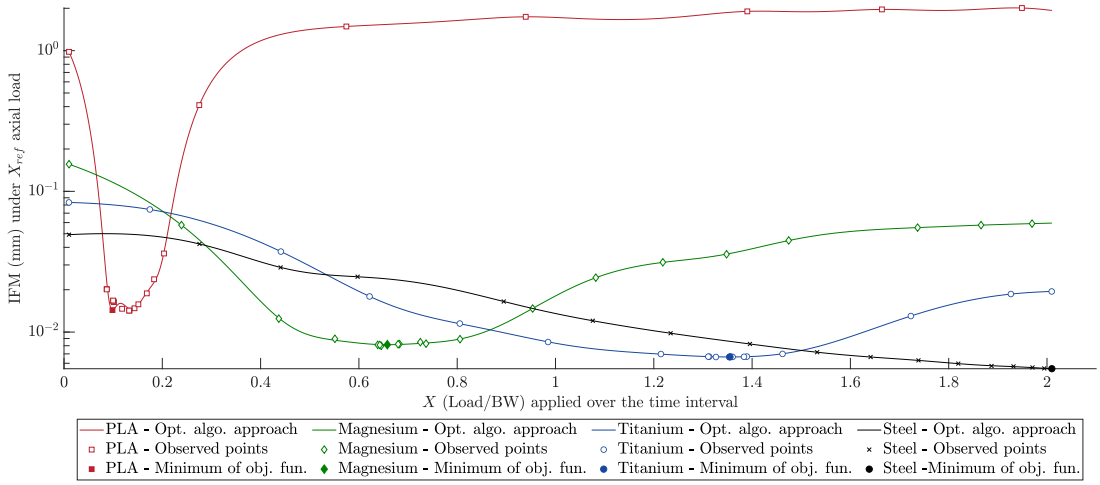

Fig. 11. Objective function exploration in the first time period, from day 1 to 30. Over the time interval, X is the axial load applied to the tibia. However, y-axis represents the IFM evaluated at the end of the time interval applying a $X_{ref} = 3$ BW.

Table 2
Optimal physiological loads applied over each simulated period and for each implant material.

Time period (days)	X (Load/BW)			
	PLA	Magnesium	Titanium	Steel
[1,30]	0.13	0.65	1.35	2.00
[31,60]	2.05	3.00	3.00	3.00

4.3. Optimisation results

The optimisation scheme (see Algorithm 1) provides the set of physiological loads which maximises the callus stiffness. Figs. 11 and 12 show the objective function exploration for each time period and implant material. The optimal values of each analysis are presented in Table 2. Then, the healing process of each optimal treatment is shown in Figs. 14 and 15. They present the bone distribution at the end of each period and a graph representing the evolution of the IFM over time for PLA, magnesium, titanium and stainless steel cases, respectively.

According to the results in Table 2 and Fig. 13, the prosthesis material's stiffness significantly affects the optimal loading pattern: the lower material stiffness, the lower the optimal load. Additionally, low implant stiffness involves a more limited range of appropriate loads since the objective function fitting shows more pronounced optimal ranges for these implant materials (see Figs. 11 and 12). This means that using an implant with high stiffness provides less sensitive outputs in terms of optimal healing outcomes and the range of feasible physiological loads.

Individually, the optimal treatment for the steel implant is based on applying high loads, as the patient could walk normally [40, 41]. This is due to the high stiffness of the implant, which allows the mechanical stimulus at the fracture site to always be low for any value of load within the possible range. Furthermore, even in the early stages of treatment, there is no risk of exceeding the

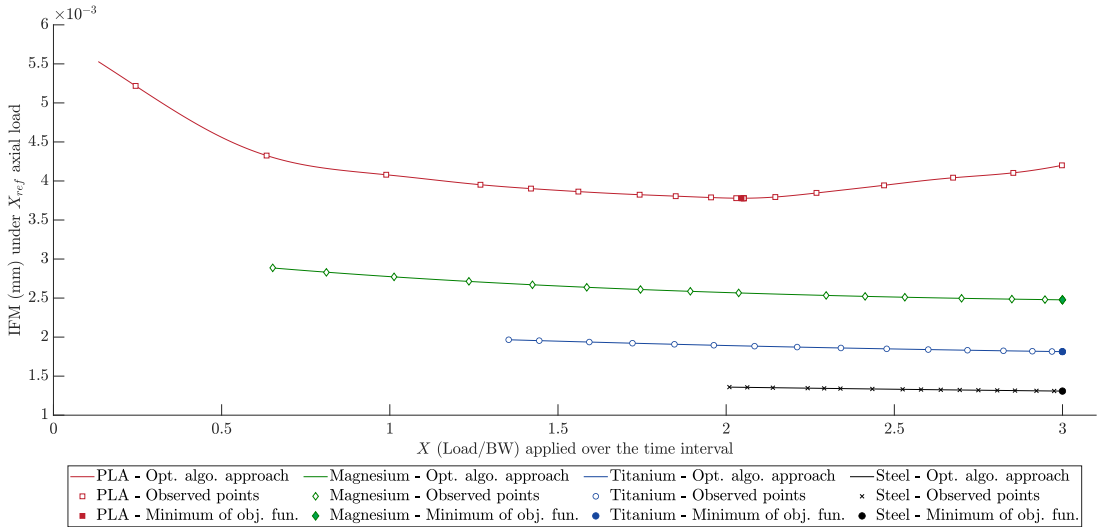

Fig. 12. Objective function exploration in the second time period, from day 31 to 61. Over the time interval, X is the axial load applied to the tibia. However, y-axis represents the IFM evaluated at the end of the time interval applying a $X_{ref} = 3$ BW.

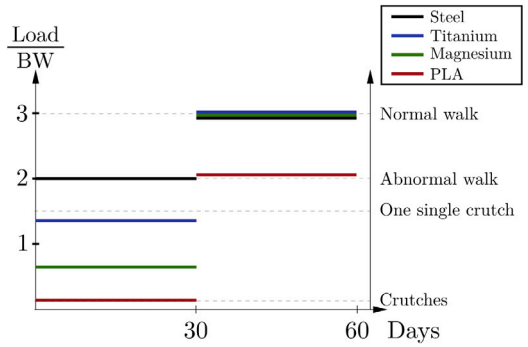

Fig. 13. Optimal physiological loads for each implant material over time and equivalent gait condition [40,41].

adequate mechanical stimulus for healing when applying high load values (see Fig. 11), This is due to the fact that the healing outcome exhibits low sensitivity in relation to the axial load when the value is within a clinical reasonable range. These findings align with those observed in conventional treatments (refer to Section 3.2).

Regarding the PLA implant, the case with the lowest stiffness, there is a range of loads that allow an optimal healing result to be obtained (see Figs. 11 and 12). In the first month, applying only 13.3% of the patient's BW is recommended, a magnitude equivalent to partial rest or walking with crutches [39,44,45]. In the second month, the ideal load increases, reaching values close to normal walking (2 times the patient's BW). However, especially in the first period, the range of proper loads is more limited than other implant materials (see Fig. 11). Consequently, this type of prosthesis requires limiting the magnitude of physiological loads, especially at early stages of recovery.

The titanium and magnesium implants offer results that combine the characteristics of the PLA and steel cases. In the first time interval, the titanium implant's ideal load is 135% of the patient's BW, close to the values recorded when walking with a single crutch (see Fig. 11). In the case of magnesium prosthesis, the optimal load is even lower (65% of BW). As a result, as in PLA case, it is necessary controlling the loading process in the first days of treatment. On the other hand, in the second month after surgery, the result is similar to steel for both materials, and the patient can walk normally (see Fig. 12).

Considering the optimal treatments from Table 2, all implant materials show similarities in the healing process when the optimal load pattern is applied (see Figs. 15 and 14). In the first time interval, the registered IFM is higher than the desired final values (when the fracture is healed) for all cases (see Fig. 15). At the beginning of this period, there is only fibrous tissue in the callus (see Fig. 14); hence, its stiffness is very low, and the prosthesis supports most of the load. The stiffness of the early callus only increases when the mechanical stimulus is in the proper range of values. Therefore, the adequate mechanical stimulus can be obtained with higher physiological forces as the stiffness increases. Consequently, the optimal physiological values are higher for the second time interval in all the case studies (see Table 2).

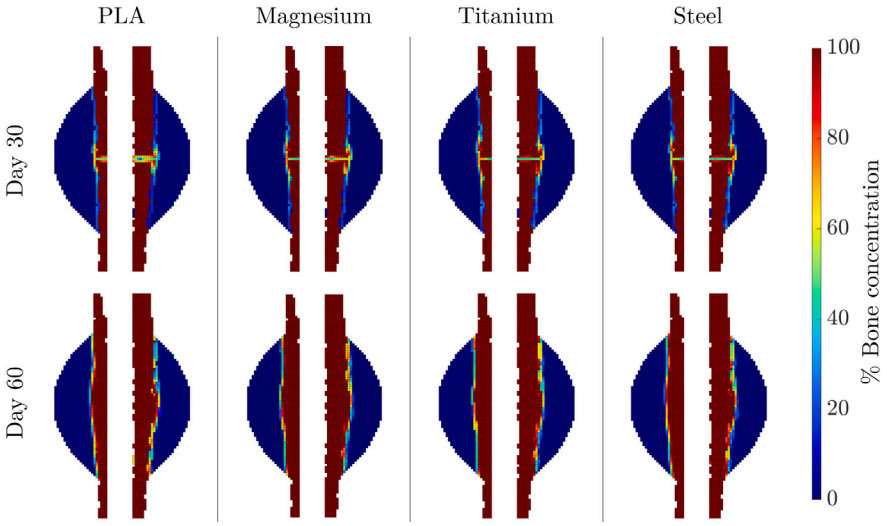

Fig. 14. Bone concentration distribution at the end of each time interval for each implant material. The distribution is represented on a slice of the sagittal plane of the tibia.

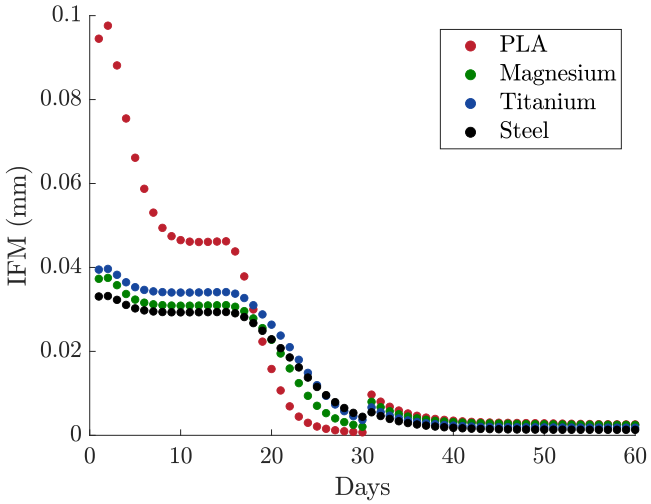

Fig. 15. IFM evolution with the optimal combination of physiological loads for each implant material.

Additionally, the stiffness increase explains the general trend of IFM evolution for all cases (see Fig. 15), reducing the vertical movement in the gap. There is a nearly plain period during the first 30 days because of the slow differentiation of new bone tissue around the gap region and the non-axisymmetric bone geometry (see Section 3.2). Only when the bone bridging is completed (union between proximal and distal bone region), the IFM is sharply reduced. In this period, the reduction of IFM in PLA implant accelerates faster than in the other analysis because of having a higher mechanical stimulus with the applied optimal load. Starting the second time interval, the IFM registers a discontinuity and a local peak in all cases due to the increase of the physiological load applied. Finally, once the bone concentration in the fracture is high, the IFM stabilises at low values, indicating a successful healing pattern.

Overall, the trend of IFM evolution and woven bone concentration is similar for all the case studies (see Figs. 14 and 15). All the cases follow similar healing patterns due to applying the optimal combination of physiological loads for each kind of prosthesis.

5. Conclusions

This work presents a methodology for developing patient-specific simulations of the bone callus healing process, which can be used to provide insights into implant design. This methodology has been used in a customised clinical treatment optimisation studying the influence of different implant materials and load conditions. The procedure is a breakthrough in this field since it combines different numerical tools to create patient-specific simulations of this biological process. To achieve this, the FE model directly considers the patient's medical image to model the geometry and mechanical properties of the bone.

Despite some simplifications in the presented study, it seems that the proposed model is sufficiently realistic to rely on its conclusions. In fact, the simulation of a conventional treatment with a stainless steel implant shows results in line with current practices and knowledge. Moreover, the presented methodology can be modified to improve the accuracy of the results obtained using more complex models or improving the FL model with more experimental data.

Using this numerical methodology, we explore the effect of different implant materials, including bioabsorbable options, on designing optimal treatments defined by load conditions. The results of load-condition optimisation study show the relationship between implant mechanical properties and required load conditions to ensure a successful healing outcome. High-stiffness implants, such as stainless steel, can tolerate high physiological loads from the beginning of treatment without severely affecting the outcome of the healing process. Conversely, low-stiffness implant materials, such as bioabsorbable PLA or magnesium, require limiting the loads applied during the early stages of treatment to obtain the appropriate mechanical stimulus in the callus region. Additionally, the healing outcome is more sensitive to the load condition in low-stiffness designs. Despite demanding more thorough control over load conditions, our findings suggest that bioabsorbable materials cannot be discarded as viable candidates for prostheses manufacturing. Further research would be interesting, particularly in light of their potential to eliminate the extraction surgery needed when conventional materials are employed.

Further research and collaboration with experimental studies are essential to validate and refine the methodology, ensuring its applicability and reliability in real-world medical scenarios. Once validated, these patient-specific simulations may provide valuable insights into the improvement of clinical treatment schemes.

CRediT authorship contribution statement

A. Martínez-Martínez: Writing – original draft, Software, Methodology, Investigation. **E. Nadal:** Supervision, Conceptualization. **D. Bonete:** Supervision. **O. Allix:** Supervision. **J.J. Ródenas:** Supervision, Conceptualization.

Declaration of competing interest

The authors declare that they have no known competing financial interests or personal relationships that could have appeared to influence the work reported in this paper.

Data availability

Data will be made available on request.

Acknowledgements

The authors gratefully acknowledge the financial support of Ministerio de Educación *y* Formación Profesional (FPU19/02103), Generalitat Valenciana, Spain (Prometeo/2021/046 and CIAICO/2021/226) and Vicerrectorado de Investigación de la Universitat Politècnica de València (PAID-11-22).

O. Allix would like to thank the French National University Council, ENS Paris-Saclay and National Center for Scientific Research (CNRS) for supporting his sabbatical at UPV, which made it possible to closely interact with the colleagues from I2MB/UPV.

Annex

In this article, the numerical mechanoregulated model presented by T. Ren [12] is used to describe the callus healing process. This method is based on previous models [5,16].

Ren's model does not consider blood perfusion as a parameters in the FLC. In other words, it considers that the whole callus region is under optimal perfusion conditions. For this reason, the validation test must be compared with T. Ren (Supplementary File 2 [12]) and U. Simon's (Figure 12 from [5]) simulation with infinity perfusion rate.

For this purpose, we replicate in this Annex the two case studies (Case A and Case B) presented by Simon, which have different loading conditions. These validation cases are inspired by previous animal experiments [4] and represent a more stable (Case A) and a less stable (Case B) fracture.

Simon explains all the parameters of these simulations in their article, but some aspects must be adapted to be implemented with our methodology. In fact, other authors modified some parameters of this numerical model to replicate Simon's results [12,46] and mention the difficulties found to replicate their model. For this reason, a detailed explanation of the followed procedure is shown in this Annex.

A.1. Geometry

Firstly, a finite element model based on Claes's [47] standard sheep tibia geometry was created to validate our model. According to Simon's implementation, Case A has a 2 mm fracture gap, and Case B has a 3 mm gap

In order to analyze this model with the cgFEM, this fractured tibia's geometry is voxelized to simulate the analysis of a medical image (see Fig. 16). The result is a 3D image of the standard tibia geometry whose voxel size is 0.25 mm in each direction.

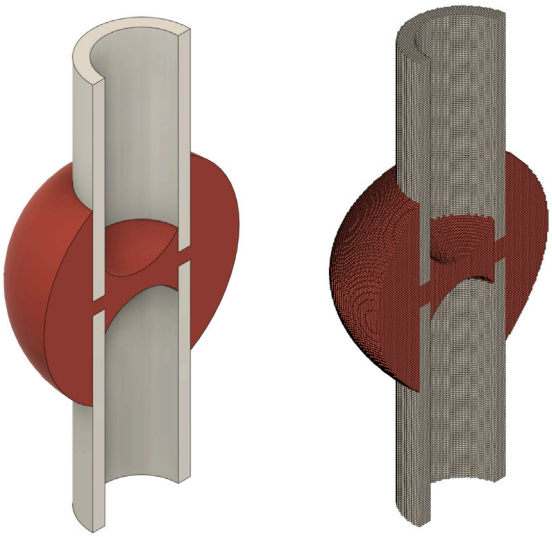

(a) 3D geometry model. (b) 3D image model.

Fig. 16. 3D image model inspired by 3D fractured tibia [47].

A.2. Boundary conditions

In animal experiments [4] used to compare and validate the model's results, a external fixator controlled the movement of the fractured bone. This fixator was modelled by Simon as a spring system. The external fixator allowed axial movement up to a maximum displacement, depending on the case study. The rest of the loads in different directions were restricted in this experiment. For this reason, there is only an axial load of 500 N on the upper surface of the cortical region. All movements are restricted on the basis of the bone.

The axial spring system is modelled parallelly to the bone's geometry. As a result, the loads supported by the whole mechanical system (bone and fixator) are always the same, but they are distributed partially to the bone depending on its global stiffness. During the first healing days, bone stiffness is low, so most of the loads are supported by the external fixator. The behaviour of the axial spring system depends on a basic stiffness $k_{bas} = 4600$ N/mm, a clearance element c (adjustable for each case study), and a return spring with a stiffness of $k_{ref} = 20$ N/mm and a pre-tension of $F_{ret} = 100$ N [4]. The maximum allowed displacement is 0.25 mm in Case A and 1.25 mm in Case B.

A.3. Mesh

Since cgFEM allows efficiently creating Cartesian meshes, an *h*-adapted mesh was used in this analysis with a voxel resolution of 0.25 mm (see Fig. 17). In the callus region, each element contains 2^3 voxels, so the element size is 0.5 mm. In the rest of the geometry, each element includes 4^3 voxels, and their size is 1 mm.

A.4. Healing model's parameters

To reduce the influence of different element sizes in the *h*-adapted mesh, all output values from the FLC are scaled by a scale factor. According to [5], the optimal tissue growth is 0.22 mm/day; consequently, the reference element size is 0.22 mm.

In the explicit temporal scheme, the time step chosen in these simulations is 1 day per iteration. This time step has provided good results and is also used in previous studies with this healing model [5,12].

The initial tissue distribution is shown in Fig. 17(a), and the mechanical properties of each tissue type are shown in Table 1. The fracture gap splits the undamaged cortical region. Around this gap, there is the callus region which is formed by connective tissue at the beginning of the simulation. As the simulations go on, voxel values or tissue concentration only updates inside the callus region.

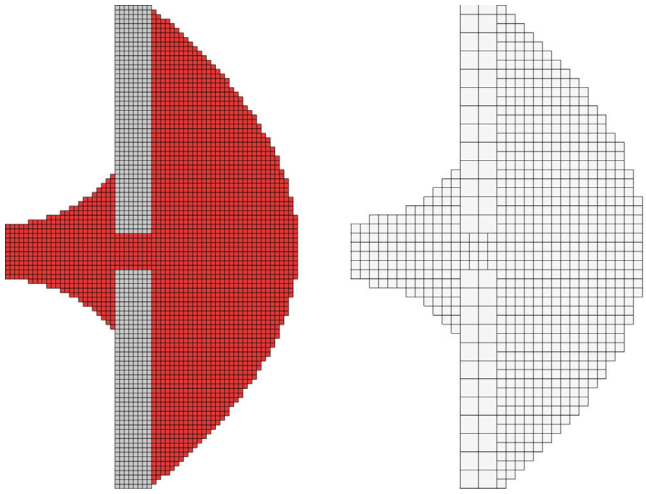

(a) 3D Image integration mesh with 0.25 mm voxel size. Callus region is in red colour and intact bone is in grey colour.

(b) 3D cartesian FEM mesh.

Fig. 17. Mesh comparison.

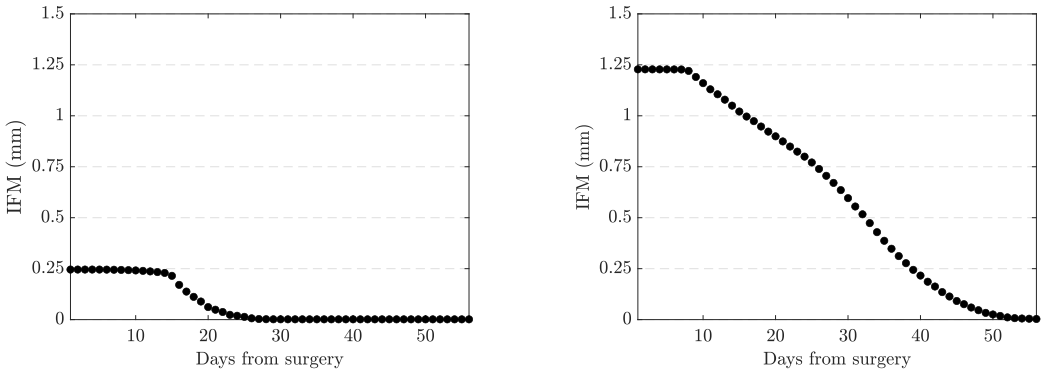

(a) Case A.

(b) Case B.

Fig. 18. Results of both validation cases using the methodology presented in this work.

A.5. Validation results

The results provided from the implementation of the FL routine in cgFEM are similar to the T. Ren's study.

IFM is the only available data to compare and validate the implementation of the callus healing model. This numerical indicator describes the healing process from a local point of view, highly depending on the tissues near the gap. Small changes in tissue differentiation might lead to differences in the IFM, so the assessment of this implementation should consider the global trend of this indicator. In fact, other authors have noted the limitations and difficulties of validating their implementations [12,13].

Our implementation has several differences from other studies which use commercial FEM software, such as the voxelization of the geometry and the use of regular hexahedral elements. Those differences can explain the slight variations in the IFM measures, but Fig. 18 shows a good correspondence with validation results in [12]. Moreover, the procedure used to measure IFM is not explained in detail in other studies.

A.6. Image resolution sensitivity

Since this work introduces a callus healing model within the context of cgFEM for the first time, it is necessary to conduct a sensitivity analysis of the discretisation employed. In our methodology, two types of discretisation are involved: the FE mesh for the mechanical problem and the 3D image for the callus healing process.

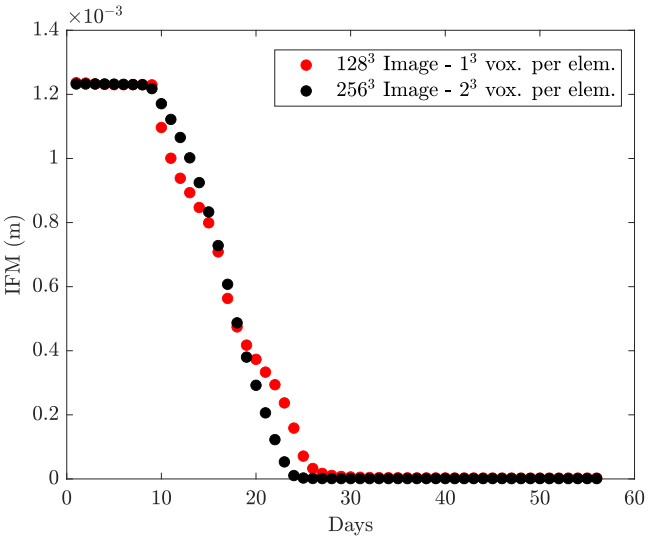

Fig. 19. Comparison of the IFM evolution for two analysis with different image resolution.

Regarding the FE mesh, the finest mesh resolution is constrained by the image resolution. In other words, the finest element of the mesh may contain only one voxel. It is worth noting that employing more elements than voxels may introduce numerical artefacts, as discussed by L. Giovannelli [19]. According to the reference, using elements that consist of 2^3 or 1^3 voxels is appropriate in terms of accuracy for the elastic problem.

On the other hand, in our methodology, the callus healing model operates at the voxel level. This implies that tissue differentiation and the evolution of mechanical properties occur at the voxel level. To mitigate the impact of image resolution dependency on the callus healing model, we have included a scaling term into our implementation, as detailed in Section 3.1.3. This approach, inspired by models based on fuzzy logic [5,12], helps reduce the influence of the mesh on the callus healing outcome.

To evaluate the sensitivity of voxel size in the callus healing model, we performed a comparative analysis utilising a standardised tibia model with a synthetic case featuring a 4 mm fracture gap, as inspired by previous works [4]. In previous studies where the callus healing model controlled the tissue concentration at the element level [5,12], sensitivity analyses were conducted using different mesh sizes. However, given that our callus healing model operates at the voxel level, we explore the effect of voxel size instead. Specifically, we compared two image-based FEM models of the same fractured tibia model, employing voxel sizes of 0.5 mm for an image resolution of 128^3 and 0.25 mm for an image resolution of 256^3. Both cases maintain the same element size while differing in voxel size. The results indicate that incorporating the scale factor reduces the mesh dependency in our methodology (see Fig. 19).

References

[1] M.S. Ghiasi, J. Chen, A. Vaziri, E.K. Rodriguez, A. Nazarian, Bone fracture healing in mechanobiological modeling: A review of principles and methods, Bone Rep. 6 (2017) 87–100, http://dx.doi.org/10.1016/j.bonr.2017.03.002, URL https://www.sciencedirect.com/science/article/pii/S2352187217300128.

[2] L. Claes, S. Recknagel, A. Ignatius, Fracture healing under healthy and inflammatory conditions, Nat. Rev. Rheumatol. 8 (2012) 133–143, http://dx.doi.org/10.1038/nrrheum.2012.1.

[3] C. Capelli, E. Sauvage, G. Giusti, G. Bosi, H. Ntsinjana, M. Carminati, G. Derrick, J. Marek, S. Khambadkone, A. Taylor, S. Schievano, Patient-specific simulations for planning treatment in congenital heart disease, Interface Focus 8 (2018) 20170021, http://dx.doi.org/10.1098/rsfs.2017.0021.

[4] L. Claes, P. Augat, G. Suger, H.-J. Wilke, Influence of size and stability of the osteotomy gap on success of fracture healing, J. Orthop. Res. : Off. Publ. Orthop. Res. Soc. 15 (1997) 577–584, http://dx.doi.org/10.1002/jor.1100150414.

[5] U. Simon, P. Augat, M. Utz, L. Claes, A numerical model of the fracture healing process that describes tissue development and revascularisation, Comput. Methods Biomech. Biomed. Eng. 14 (1) (2011) 79–93, http://dx.doi.org/10.1080/10255842.2010.499865, arXiv:https://doi.org/10.1080/10255842.2010.499865. PMID: 21086207.

[6] R. Fu, Y. Feng, Y. Liu, B.M. Willie, H. Yang, The combined effects of dynamization time and degree on bone healing, J. Orthop. Res. 40 (3) (2022) 634–643, http://dx.doi.org/10.1002/jor.25060, arXiv:https://onlinelibrary.wiley.com/doi/pdf/10.1002/jor.25060. URL https://onlinelibrary.wiley.com/doi/abs/10.1002/jor.25060.

[7] H. Isaksson, Recent advances in mechanobiological modeling of bone regeneration, Mech. Res. Commun. 42 (2012) 22–31, http://dx.doi.org/10.1016/j.mechrescom.2011.11.006, URL https://www.sciencedirect.com/science/article/pii/S0093641311002187. Recent Advances in the Biomechanics of Growth and Remodeling.

[8] A. Goodship, J. Kenwright, The influence of induced micromovement upon the healing of experimental tibial fractures, J. Bone Joint Surg. Br. 67 (1985) 650–655, http://dx.doi.org/10.3928/0147-7447-19840301-14.

[9] C.J. Moran, A. Ramesh, P.A. Brama, J.M. O'Byrne, F.J. O'Brien, T.J. Levingstone, The benefits and limitations of animal models for translational research in cartilage repair, J. Exp. Orthop. 3 (1) (2016) 1–12.

[10] L. Claes, Improvement of clinical fracture healing – what can be learned from mechano-biological research? J. Biomech. 115 (2021) http://dx.doi.org/10.1016/J.JBIOMECH.2020.110148.

[11] D. Lacroix, P. Prendergast, A mechano-regulation model for tissue differentiation during fracture healing: analysis of gap size and loading, J. Biomech. 35 (9) (2002) 1163–1171, http://dx.doi.org/10.1016/S0021-9290(02)00086-6, URL https://www.sciencedirect.com/science/article/pii/S0021929002000866.

[12] T. Ren, H. Dailey, Mechanoregulation modeling of bone healing in realistic fracture geometries, Biomech. Model. Mechanobiol. 19 (2020) http://dx.doi.org/10.1007/s10237-020-01340-5.

[13] T. Wehner, L. Claes, F. Niemeyer, D. Nolte, U. Simon, Influence of the fixation stability on the healing time—a numerical study of a patient-specific fracture healing process, Clin. Biomech. 25 (6) (2010) 606–612.

[14] M. Steiner, L. Claes, A. Ignatius, F. Niemeyer, U. Simon, T. Wehner, Prediction of fracture healing under axial loading, shear loading and bending is possible using distortional and dilatational strains as determining mechanical stimuli, J. R. Soc. Interface 10 (86) (2013) 20130389.

[15] C. Quinn, A. Kopp, T.J. Vaughan, A coupled computational framework for bone fracture healing and long-term remodelling: Investigating the role of internal fixation on bone fractures, 2021.

[16] S.J. Shefelbine, P. Augat, L. Claes, U. Simon, Trabecular bone fracture healing simulation with finite element analysis and fuzzy logic, J. Biomech. 38 (12) (2005) 2440–2450, http://dx.doi.org/10.1016/j.jbiomech.2004.10.019, URL https://www.sciencedirect.com/science/article/pii/S0021929004005159.

[17] A. Düster, E. Rank, B. Szabó, The p-version of the finite element and finite cell methods, in: Encyclopedia of Computational Mechanics Second Edition, John Wiley & Sons, Ltd Chichester, UK, 2017, pp. 1–35.

[18] E. Burman, S. Claus, P. Hansbo, M.G. Larson, A. Massing, CutFEM: discretizing geometry and partial differential equations, Internat. J. Numer. Methods Engrg. 104 (7) (2015) 472–501.

[19] L. Giovannelli, J. Ródenas, J. Navarro-Jiménez, M. Tur, Direct medical image-based finite element modelling for patient-specific simulation of future implants, Finite Elem. Anal. Des. 136 (2017) 37–57, http://dx.doi.org/10.1016/j.finel.2017.07.010.

[20] M. Ruess, D. Tal, N. Trabelsi, Z. Yosibash, E. Rank, The finite cell method for bone simulations: verification and validation, Biomech. Model. Mechanobiol. 11 (3) (2012) 425–437.

[21] S. Claus, P. Kerfriden, F. Moshfeghifar, S. Darkner, K. Erleben, C. Wong, Contact modeling from images using cut finite element solvers, Adv. Model. Simul. Eng. Sci. 8 (1) (2021) 1–23.

[22] J. Gutiérrez-Gil, E. Nadal, K. Bouza, M. Tur, C. Atienza, O. Allix, J. Ródenas, Bone remodelling-based numerical evaluation of personalized masticatory forces from CT-scans, Comput. Methods Appl. Mech. Engrg. 401 (2022) 115635.

[23] C. Capelli, E. Sauvage, G. Giusti, G. Bosi, H. Ntsinjana, M. Carminati, G. Derrick, J. Marek, S. Khambadkone, A. Taylor, S. Schievano, Patient-specific simulations for planning treatment in congenital heart disease, Interface Focus 8 (2018) 20170021, http://dx.doi.org/10.1098/rsfs.2017.0021.

[24] M. Viceconti, M. Qasim, P. Bhattacharya, X. Li, Are CT-based finite element model predictions of femoral bone strengthening clinically useful? Curr. Osteoporos. Rep. 16 (3) (2018) 216–223.

[25] H.S. Hosseini, A. Dünki, J. Fabech, M. Stauber, N. Vilayphiou, D. Pahr, M. Pretterklieber, J. Wandel, B. van Rietbergen, P.K. Zysset, Fast estimation of Colles' fracture load of the distal section of the radius by homogenized finite element analysis based on HR-pQCT, Bone 97 (2017) 65–75, http://dx.doi.org/10.1016/j.bone.2017.01.003, URL https://www.sciencedirect.com/science/article/pii/S8756328217300030.

[26] D.-S. Son, H. Mehboob, H.-J. Jung, S.-H. Chang, The finite element analysis for endochondral ossification process of a fractured tibia applied with a composite IM-rod based on a mechano-regulation theory using a deviatoric strain, Compos. B (2013) http://dx.doi.org/10.1016/j.compositesb.2013.08.004.

[27] D.R. Carter, G.S. Beaupré, N.J. Giori, J.A. Helms, Mechanobiology of skeletal regeneration, Clin. Orthop. Relat. Res. (1998) S41–S55.

[28] C. Ament, E. Hofer, A fuzzy logic model of fracture healing, J. Biomech. 33 (8) (2000) 961–968, http://dx.doi.org/10.1016/S0021-9290(00)00049-X, URL https://www.sciencedirect.com/science/article/pii/S002192900000049X.

[29] D. Muñoz, J. Albelda, J.J. Ródenas, E. Nadal, Improvement in 3D topology optimization with h-adaptive refinement using the cartesian grid finite element method, Internat. J. Numer. Methods Engrg. 123 (13) (2022) 3045–3072.

[30] C.-C. Lee, Fuzzy logic in control systems: fuzzy logic controller. I, IEEE Trans. Syst. Man Cybern. 20 (2) (1990) 404–418.

[31] Tibia post traumatic deformity 1.0.0, 2022, https://www.embodi3d.com/files/file/53336-tibia-post-traumatic-deformity/. Accessed: 2022-11-25.

[32] H. Wang, Z. Hao, S. Wen, Finite element analysis of the effect of medullary contact on fracture healing and remodeling in the intramedullary interlocking nail-fixed tibia fracture, Int. J. Numer. Methods Biomed. Eng. 33 (2016) http://dx.doi.org/10.1002/cnm.2816.

[33] M. Pérez, P. Fornells, J. García-Aznar, M. Doblaré, Validation of Bone Remodelling Models Applied to Different Bone Types Using Mimics, University of Zaragoza, 2007.

[34] E. Schileo, F. Taddei, A. Malandrino, L. Cristofolini, M. Viceconti, Subject-specific finite element models can accurately predict strain levels in long bones, J. Biomech. 40 (13) (2007) 2982–2989, http://dx.doi.org/10.1016/j.jbiomech.2007.02.010, URL https://www.sciencedirect.com/science/article/pii/S0021929007000711.

[35] L. Peng, J. Bai, X. Zeng, Y. Zhou, Comparison of isotropic and orthotropic material property assignments on femoral finite element models under two loading conditions, Med. Eng. Phys. 28 (3) (2006) 227–233.

[36] T.S. Keller, Predicting the compressive mechanical behavior of bone, J. Biomech. 27 (9) (1994) 1159–1168.

[37] N.K. Knowles, J.M. Reeves, L.M. Ferreira, Quantitative computed tomography (QCT) derived bone mineral density (BMD) in finite element studies: a review of the literature, J. Exp. Orthop. 3 (2016) 1–16.

[38] B.J. Braun, M. Orth, S. Diebels, K. Wickert, A. Andres, J. Gawlitza, A. Bücker, T. Pohlemann, M. Roland, Individualized determination of the mechanical fracture environment after tibial exchange nailing—A simulation-based feasibility study, Front. Surg. 8 (2021) http://dx.doi.org/10.3389/fsurg.2021.749209, URL https://www.frontiersin.org/article/10.3389/fsurg.2021.749209.

[39] H. Mehboob, S.H. Chang, Evaluation of healing performance of biodegradable composite bone plates for a simulated fractured tibia model by finite element analysis, Compos. Struct. 111 (2014) 193–204, http://dx.doi.org/10.1016/j.compstruct.2013.12.013.

[40] A. Mehboob, H. Mehboob, S.-H. Chang, F. Tarlochan, Effect of composite intramedullary nails (IM) on healing of long bone fractures by means of reamed and unreamed methods, Compos. Struct. 167 (2017) 76–87, http://dx.doi.org/10.1016/j.compstruct.2017.01.076, URL https://www.sciencedirect.com/science/article/pii/S0263822316330094.

[41] J. Nourisa, G. Rouhi, Biomechanical evaluation of intramedullary nail and bone plate for the fixation of distal metaphyseal fractures, J. Mech. Behav. Biomed. Mater. 56 (2016) 34–44, http://dx.doi.org/10.1016/j.jmbbm.2015.10.029, URL https://www.sciencedirect.com/science/article/pii/S1751616115004154.

[42] V. Tsakiris, C. Tardei, F.M. Clicinschi, Biodegradable Mg alloys for orthopedic implants – A review, J. Magnes. Alloys 9 (2021) 1884–1905, http://dx.doi.org/10.1016/J.JMA.2021.06.024.

[43] C.C. Barber, M. Burnham, O. Ojameruaye, M.D. McKee, A systematic review of the use of titanium versus stainless steel implants for fracture fixation, OTA Int. 4 (3) (2021).

[44] H.J. Kim, S.H. Chang, H.J. Jung, The simulation of tissue differentiation at a fracture gap using a mechano-regulation theory dealing with deviatoric strains in the presence of a composite bone plate, Composites B 43 (2012) 978–987, http://dx.doi.org/10.1016/j.compositesb.2011.09.011.

[45] S. Heintz, E.M. Gutierrez-Farewik, Static optimization of muscle forces during gait in comparison to EMG-to-force processing approach, Gait Posture 26 (2) (2007) 279–288, http://dx.doi.org/10.1016/j.gaitpost.2006.09.074, URL https://www.sciencedirect.com/science/article/pii/S0966636206002815.

[46] C. Wilson, M. Schutz, D. Epari, Computational simulation of bone fracture healing under inverse dynamization, Biomechanics and modeling in mechanobiology 16 (2017) 5–14, http://dx.doi.org/10.1007/s10237-016-0798-x.

[47] L. Claes, C. Heigele, Magnitudes of local stress and strain along bony surfaces predict the course and type of fracture healing, J. Biomech. 32 (3) (1999) 255–266, http://dx.doi.org/10.1016/S0021-9290(98)00153-5, URL https://www.sciencedirect.com/science/article/pii/S0021929098001535.